

On the structural integrity of Fe-36Ni Invar alloy processed by selective laser melting

T. Wegener^{1*}, F. Brenne², A. Fischer¹, T. Möller³, C. Hauck⁴, S. Auernhammer⁴, T. Niendorf¹

¹ *Institut für Werkstofftechnik, Metallische Werkstoffe, Universität Kassel, Mönchebergstraße 3, 34125 Kassel, Deutschland*

² *Department of Mechanical Science and Engineering, University of Illinois at Urbana-Champaign, 1206 West Green Street, Urbana, IL 61801, USA*

³ *Carl Zeiss SMT GmbH, Rudolf-Eber-Straße 2, 73447 Oberkochen, Deutschland*

⁴ *MBFZ toolcraft GmbH, Handelsstraße 1, 91166 Georgensgmünd*

Abstract

Specimens made from pre-alloyed Invar (Fe-36Ni) powder were fabricated by selective laser melting and stress-relief heat treated afterwards. A density of the fabricated parts of 99.6 % was determined by computed tomography. The microstructure and mechanical behavior under monotonic and particularly cyclic loading at ambient temperature were investigated. Results reveal a bimodal microstructure containing columnar and equiaxed grains with an average grain size of 75 μm and pronounced texture $\langle 001 \rangle \parallel \text{BD}$. The selective laser melted Invar is characterized by a homogeneous hardness distribution revealing no gradient with respect to the height of the fabricated parts. The mechanical response under monotonic tensile loading is characterized by a fairly ductile behavior. Total strain controlled low-cycle fatigue tests with varying strain amplitudes were performed. The cyclic deformation response is characterized by highly reproducible behavior in terms of stress amplitudes and number of cycles to failure. The corresponding half-life hysteresis loops reveal perfect Masing behavior. Post-mortem fractography revealed crack initiation in direct vicinity of the surfaces. The damage tolerance of Invar is found to be promoted by its high ductility. Finally, a low coefficient of thermal expansion,

very similar to conventionally processed Invar, was shown by dilatometer tests in the temperature range between 0°C-180 °C.

Keywords: Invar 36, Additive Manufacturing, Selective Laser Melting, Low-Cycle Fatigue, Microstructure

1. Introduction

Fe-rich, face centered cubic (fcc) Fe-Ni alloys with a Ni content of 30 to 40 mass% are well-known for their low coefficients of thermal expansion (CTEs) near room temperature [1,2]. The physical origin of this phenomenon can be explained by a spontaneous volume magnetostriction, i.e., the compensation of lattice shrinkage with decreasing temperature by the lattice expansion due to the onset of ferromagnetism below the Curie Temperature (T_C) [3]. Above T_C the ferromagnetic behavior changes to a completely paramagnetic behavior resulting in normal thermal expansion.

The lowest CTE ($< 2 \times 10^{-6} \text{ K}^{-1}$) in the Fe-Ni system can be found in the single γ -phase $\text{Fe}_{64}\text{Ni}_{36}$ alloy composition. Due to its *invariant* length with respect to a temperature change, this alloy, discovered by Guillaume in 1898, is better known as Invar 36 or Invar alloy [1]. The anomalous and unique properties of Invar are often referred to as the Invar effect.

Besides the high scientific interest, Invar is the material of choice for numerous applications in a wide variety of areas. Due to its low CTE and excellent mechanical properties in cryogenic environment it is commonly used as a high precision and highly reliable material in components where superior dimensional stabilities are required, e.g. aerospace control devices, metrology equipment, clocks, precision instruments, shadow masks, liquefied natural gas containers and storage tanks [1,2,4–7]. Invar components are conventionally manufactured by mechanical processes such as machining and rolling or by electroforming [8]. As a result of high ductility and pronounced work hardening in combination with a low heat conductivity the machinability of Invar is challenging, i.e., the increased tool wear causes high production costs and a low efficiency [9–12]. These problems become extremely challenging when machining of complex precision components is required.

Selective Laser Melting (SLM), a powder-bed based Additive Manufacturing (AM) technology, represents one of the most powerful and promising candidates to overcome the

challenges related to conventional machining of the Invar alloy. The SLM process enables a tool-free near-net shape production of complex freeform components, near-fully dense directly from a computer-aided design (CAD) model. It is based on the consecutive consolidation of metallic powders by a high-power laser and the repetitive fusing of thin layers on top of each other providing unprecedented design freedom as compared to conventional manufacturing techniques [13–16]. Typical applications of SLM-components are in the biomedical field, e.g., for dental crowns made of cobalt-chromium alloys or as patient-specific implants made of Ti-6Al-4V, the most commonly used material in powder-bed based AM so far [17,18]. Furthermore, due to the high degree of design freedom, the SLM technology offers the possibility of producing very complex lightweight structures. Thus, a great potential is seen for the technology, particularly in the aerospace sector [19].

The majority of the studies reporting on additively manufactured Invar focused on the general processability, thermal expansion behavior and microstructure evolution. Comparable to numerous other studies on additively processed materials [20–22], the influence of different process parameters was likewise focus of several investigations. Qui et al. [7] studied the microstructure and properties of selective laser melted Invar 36 revealing very low porosity ($< 0.5\%$) for laser scanning speeds below 3200 mm/s and a microstructure in the as-built condition composed of columnar γ -grains oriented alongside the build direction (BD) decorated by α -precipitates. Moreover, development of a strong near $\langle 001 \rangle$ texture could be observed. Anisotropic tensile behavior was reported for the as-built Invar 36 with horizontally built specimens (loading direction \perp BD) displaying superior ultimate strength (UTS) and yield strength (YS) as compared to their vertically built counterparts (loading direction \parallel BD). In contrast, elongation at failure was superior for the latter condition as a result of shear deformation instead of intergranular failure seen for the horizontally built specimens. Authors further focused on the effect of post-processing heat treatment showing that hot isostatic pressing (HIP), performed at 950 °C and 100 MPa for 2 h, led to a significant decrease of strength and ductility due to coarsening of the α -precipitates mainly along the grain boundaries. Post-SLM heat treatment without pressure (830 °C for 0.5 h followed by water quenching + 570 °C for 1 h followed by air cooling + 95 °C for 48 h) did not influence tensile properties as a result of insignificant changes in the microstructure. Irrespective of post-processing treatment low CTEs below 300° C, similar to conventionally manufactured Invar 36, were reported. Harrison et al. [23] focused in their study on thermal expansion coefficients of SLM processed Invar. They reported near-fully dense components in the as-built condition displaying tensile properties similar to cold-drawn, and superior to annealed Invar. Besides, the as-built material

exhibited a lower thermal expansion coefficient than conventionally manufactured Invar and residual stress was found to be a significant contributor to this decrease in the CTE. Moreover the authors observed a slight anisotropy in CTE values with respect to the building direction (parallel and normal), that was ascribed to a heterogeneous distribution of defects such as micropores and microcracks within the as-built components.

Several investigations on selective laser melted Invar 36 were published by the group of Yakout et al. [12,24,25]. In their first study focusing on optimization of process parameters a strong influence of the laser energy density on the density of the parts produced was reported, i.e., up to a certain limit the density of the fabricated parts increases as the energy density increases. However, after reaching this limit the quality of the fabricated parts starts to deteriorate due to thermal and residual stresses. As a result a laser energy density range of approximately 60 to 75 J/mm³ was recommended [12]. A second study of Yakout et al. [24] focused on CTE and microstructure evolution of Invar and stainless steel 316L. A critical energy density of $E_C = 86.6 \text{ J/mm}^3$ was reported for Invar. For laser energy densities $< E_C$ void formation and, as a consequence, a reduced CTE, that in general was found to be similar to conventionally processed material, was shown. Laser energy densities higher than E_C were found to lead to vaporization and microsegregation of some elements resulting in a reduced CTE value. In their latest study density and mechanical properties of SLM Invar and stainless steel 316L were studied in depth [25]. A brittle-ductile transition linked to a critical energy density of $E_T = 52.1 \text{ J/mm}^3$ was found for Invar. A brittle fracture behavior due to void formation was shown for all energy densities below this threshold. Furthermore, highest density and toughness as well as medium residual stresses were reported for laser energy densities in the range $E_T < E < E_C$. Differing mechanical properties due to changes in the chemical composition were observed for laser energy densities $> E_C$.

The results of Yakout et al. are in line with the investigations of Asgari et al. [9] focusing on the CTE behavior of Invar alloy fabricated by modulated laser powder bed fusion. They showed that an increase in laser power results in a decreasing volume fraction of pores and concomitantly to strengthening of the $\langle 110 \rangle$ texture component parallel to the building direction. Thermal expansion behavior was found to be similar to that of conventionally manufactured Invar. However, thermal expansion displacement increased with decreasing porosity and a more pronounced $\langle 110 \rangle$ texture component parallel to the building direction, respectively.

Density and surface roughness characteristics of Invar during selective laser sintering were investigated by Khanna et al. [26]. The layer thickness was found to be the most influential process parameter on both surface roughness and density. Besides, a linear relationship was

observed between the density and surface roughness and the energy density applied. In line with the results of the aforementioned studies, the authors found that the density of the printed components increases with increased energy density, whereas the surface roughness decreases at the same time. The latter phenomenon was explained by powder particles adhering to the outer surface of the printed parts as a result of increased thermal input. Small voids and pores were found to be the most dominant defects in the parts of highest density, while the least dense parts were characterized by lack-of-fusion and balling phenomena due to insufficient energy input. Based on all results obtained the authors recommended optimized process parameters for achieving balanced properties with respect to density and surface roughness.

A very recent study exploring the influence of process parameters on the microstructure and mechanical properties of Invar alloy additively manufactured by selective laser melting using an island strategy was published by Wei et al. [27]. An optimal energy density of $E_V = 99.2 \text{ J/mm}^3$, resulting in as-fabricated Invar parts with a density of 99.5 %, a Vickers hardness of 1.8 GPa and ultimate tensile strength of 480 MPa, was recommended. Processing with energy densities below the recommended optimum ($E_V = 23.5$ and 55.5 J/mm^3) resulted in lack-of fusion pores, unmelted powder particles and blurry boundaries of islands whereas using a higher energy density of $E_V = 198.4 \text{ J/mm}^3$ induced keyhole pores as well as irregular boundaries between individual islands. Furthermore, as-fabricated parts mainly consisted of γ and α phases.

The fatigue properties of SLM-processed Invar have not been addressed so far. At this point only one study focusing on the fatigue life of conventionally processed Invar is available in literature. Vinogradov et al. [28] reported on the fatigue life of coarse grained Invar and its ultra-fine grained counterparts in the low cycle fatigue (LCF) and high cycle fatigue (HCF) regime, respectively.

In light of the findings presented the general processability of dense Invar components by SLM has been affirmed. However, reports detailed above only investigate process parameter optimization, microstructure evolution, post-processing treatments and thermal expansion behavior. The mechanical behavior is barely studied. To the best of the authors' knowledge investigations on the mechanical behavior of SLM-processed Invar, especially in terms of fatigue, are lacking.

Data available in literature reporting on AM metals in general show that multiple parameters, i.e., build direction, surface roughness, residual stresses, heat treatment and most importantly microstructural defects such as pores and lack of fusion, affect the fatigue behavior of AM components [29]. Since many components made of Invar, e.g. precision optics

instruments, are employed under very complex loading regimes, often including cyclic loads, the performance under fatigue loading needs to be investigated thoroughly.

In order to close prevalent research gaps and pave the way for robust assessment of structural integrity and wide acceptance of selective laser melted Invar components, even in sophisticated fatigue loaded applications, the current study was conducted. As is highlighted in the introduction section, the influence of different process parameters on resulting microstructure and mechanical properties has already been comprehensively characterized for SLM-processed Invar. However, as the introduction further clearly outlines, none of the studies published to date has investigated the fatigue behaviour of SLM-manufactured Invar. Based on the results in literature only one set of parameters was chosen and employed to obtain novel insights into the performance of SLM-processed Invar under cyclic loading. Invar components were processed by selective laser melting and the microstructure was studied comprehensively by scanning electron microscopy (SEM) and computed tomography (CT). The main objective of the current investigation is the analysis of the mechanical behavior, particularly the fatigue behavior in the LCF regime, representing a novelty in literature that needs to be addressed. Results are critically discussed based on microstructure details and fracture surface analysis. Furthermore, thermal expansion behavior is studied in order to assess the most important property of the Invar alloy. Thereby, the overall suitability of SLM-processed Invar for industry applications, even in the case of cyclically loaded components, is definitely established.

2. Material and methods

Cuboids with the dimension of 20 mm × 10 mm × 31 mm (cf. Fig 1 a)) were built using gas-atomized Invar powder. By analysis of particle size distribution conducted using a Malvern Morphologi G3SE high resolution microscope, values of d_{10} , d_{50} and d_{90} were determined as 13, 29 and 40 μm , respectively. The chemical composition (in wt.%) of the precursor powder as provided by the powder manufacturer is given in table 1.

The cuboids were manufactured using a TruPrint 1000 machine (Trumpf GmbH + Co. KG, Germany) equipped with a 200 W fibre laser. Prior to fabrication of the cuboids optimized SLM processing parameters were determined via a statistical design of experiment (DoE). In this DoE the laser power, scan speed and hatch distance were varied in order to eventually allow for production of dense parts being characterized by minimum defect density. As a result, the following values were set as process parameters using a chessboard scanning strategy: layer

thickness 30 μm and hatch distance 0.105 mm. The fibre laser was operated with a spot size of 75 μm at a speed of 900 mm/s and a power of 200 W, resulting in an energy density of approximately 70.5 J/mm³. Furthermore, no additional platform heating was used and argon was employed as process gas.

Table 1 Chemical composition of the precursor powder material (in wt.%)

Element	Fe	Ni	Mn	C	N	O	Si
wt.%	Bal.	35.81	0.47	0.0032	0.0059	0.00156	< 0.01

For microstructure analysis and mechanical characterization flat dog bone shape specimens with a nominal gauge section of 8 mm \times 3 mm \times 1.5 mm (displayed in Fig. 1b) were cut from the cuboids by electro-discharge machining (EDM). In accordance with the schematic shown in Fig. 1a the specimens were taken from the center of the cuboids in order to avoid any influences caused by surface or edge effects and to ensure a homogeneous microstructure within the entire gauge section. The loading direction of the specimens corresponds to the build direction of the cuboids. Upon processing and EDM all specimens were subjected to a three-step annealing heat-treatment shown in Fig. 1c (in the remainder of this paper the corresponding condition is referred to as SLM Invar). The heat-treatment chosen is not standard, however, in preliminary experiments it was found that the treatment is able to relieve all residual stresses without significant changes in microstructure.

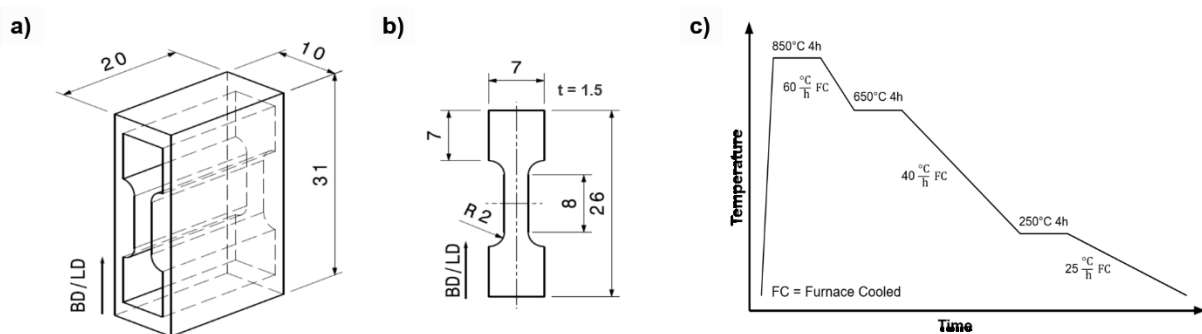


Fig. 1 (a) Schematic depicting the processed cuboids highlighting the location of the specimens; (b) geometry of tensile and fatigue specimens; (c) schematic representation of the heat treatment process considered in present work. The building direction / loading direction is indicated by the arrow “BD/LD”.

In order to guarantee a high surface quality, all specimens were mechanically ground down after fabrication and post-processing to 5 μm grit size using SiC paper. Microstructure analysis was carried out using a Zeiss ULTRA GEMINI high-resolution SEM operating at 30 kV. The SEM system is equipped with a back-scattered electron (BSE) detector and an electron back-scatter diffraction (EBSD) unit. Energy dispersive X-ray spectroscopy (EDS) method was used to analyze the final chemical composition. For BSE and EBSD measurements specimens were vibration polished for 12 hours using conventional oxide polishing suspension (OPS) with a grain size of 0.04 μm . Fracture surface investigations after tensile and fatigue testing were conducted using a second SEM system (CamScan MV 2300) operating at an acceleration voltage of 20 kV. Texture analysis was done by X-ray diffraction (XRD) using an Empyrean X-ray diffractometer (Panalytical GmbH, Germany) operating at 40 kV. Three planes of the fcc phase, i.e., $\{111\}$, $\{200\}$ and $\{220\}$ have been considered for these measurements. The MATLAB™ toolbox MTEX was used for evaluation of data [30]. In MTEX an entirely random texture will have an orientation distribution function (ODF) being equal to one. In other words, the values of ODFs and, thus, inverse pole figures (IPFs) in MTEX can be interpreted as multiples of the random distribution (mrd).

For the three-dimensional-non-destructive defect characterization a Zeiss Xradia 520 Versa μ -Computertomograph (μ -CT) was used operating at a voltage of 40 kV and a power of 3 W. During a measurement, the detector captures several 2D projection images of the 360° rotating sample, which are reconstructed into a 3D-data set of voxels. The average pore diameter was calculated based on comprehensive micrograph analysis. On this basis, a very fine voxel size of 1.95 μm was applied, which enables a reliable determination of the prevailing porosity. Evaluation of the measurements was done using the rendering software Avizio 9.4.0. Due to the very high resolution, the prevailing porosity is determined with high accuracy. Noise reduction was carried out by an appropriate filter (Non-Local-Means Filter), so that the error deviation could be reduced to a minimum. For details on data analysis the reader is referred to [31]. In order to ensure full penetration of the X-rays, a μ -CT specimen with dimensions of 1 mm \times 1.3 mm \times 10 mm has been cut from the gauge length of a virgin tensile specimen by EDM.

Vickers hardness testing was carried out on a Struers DuraScan-70 system employing a load of 9.81 N. Thermal expansion measurement was performed on a cylindrical sample oriented parallel to the build direction with a diameter of 4 mm and a length of 25 mm between 0 °C and 180 °C using a Netzsch DIL 402C vacuum-tight pushrod dilatometer. The specimen, taken from the center of the SLM processed cuboid by EDM, was initially cooled down from

room temperature ($T_0 = 21\text{ }^\circ\text{C}$) to $0\text{ }^\circ\text{C}$ and subsequently heated to $180\text{ }^\circ\text{C}$ with a $1\text{ }^\circ\text{C}/\text{min}$ heating rate.

Uniaxial room temperature tensile tests were conducted using a screw-driven MTS Criterion load frame with a maximum loading capability of 20 kN. The tests were performed in displacement control with a constant crosshead speed of 2 mm/min. Nominal stress-strain diagrams were plotted based on the load and displacement signals as well as the gauge section dimensions as given in Fig. 1b. LCF experiments were carried out at ambient temperature using a digitally controlled servo-hydraulic load frame with a maximum force of 16 kN. For these tests a MTS miniature extensometer with a gauge length of 3 mm was directly attached to the surface of the specimens. The low-cycle fatigue tests were performed in fully reversed push-pull loading ($R_\epsilon = -1$) in strain control with a constant strain rate of $6 \times 10^{-3}\text{ s}^{-1}$ and total strain amplitudes of $\Delta\epsilon/2 = \pm 0.35\%$, $\Delta\epsilon/2 = \pm 0.5\%$ and $\Delta\epsilon/2 = \pm 0.65\%$. These total strain amplitudes were chosen based on commonly used values for investigations in the LCF regime in literature [32–34].

3. Results

3.1 Microstructural characterization

The final chemical composition of the heat-treated specimens was determined by EDS. The investigation focused on the main elements Fe, Ni and Mn as shown for the chemical composition of the precursor powder in table 1, other elements were not considered. According to results obtained by EDS the final chemical composition in wt.% was 62.8%, 36.54% and 0.66% for Fe, Ni and Mn, respectively.

Representative BSE micrographs of the SLM Invar specimens for two different magnifications, i.e., $250\times$ and $1000\times$, are presented in Fig. 2a and b, respectively. From both images a homogeneous microstructure evolution during processing without the presence of any segregations can be seen. However, spherical defects (highlighted by the red circles) can be seen in both micrographs. With respect to grain morphology, the microstructure is regarded as bimodal, being characterized by fan-like grain clusters consisting of a mixture of columnar and globular grains, highlighted by the white and red rectangles, respectively.

These findings are confirmed by the EBSD measurements. Fig. 3 shows a representative EBSD image quality map (a) and the corresponding inverse pole figure map (b) of the SLM

processed Invar. The image quality map clearly indicates the bimodal nature of the microstructure consisting of columnar as well as globular grains. In some areas the columnar grains have grown epitaxially across several layers. The average grain size was found to be approximately 75 μm . From the corresponding inverse pole figure map in (b) the texture development can be analyzed. Deduced from the relatively high fraction of $\langle 001 \rangle$ orientated grains displayed in red, a strong texture with respect to the build direction is found.

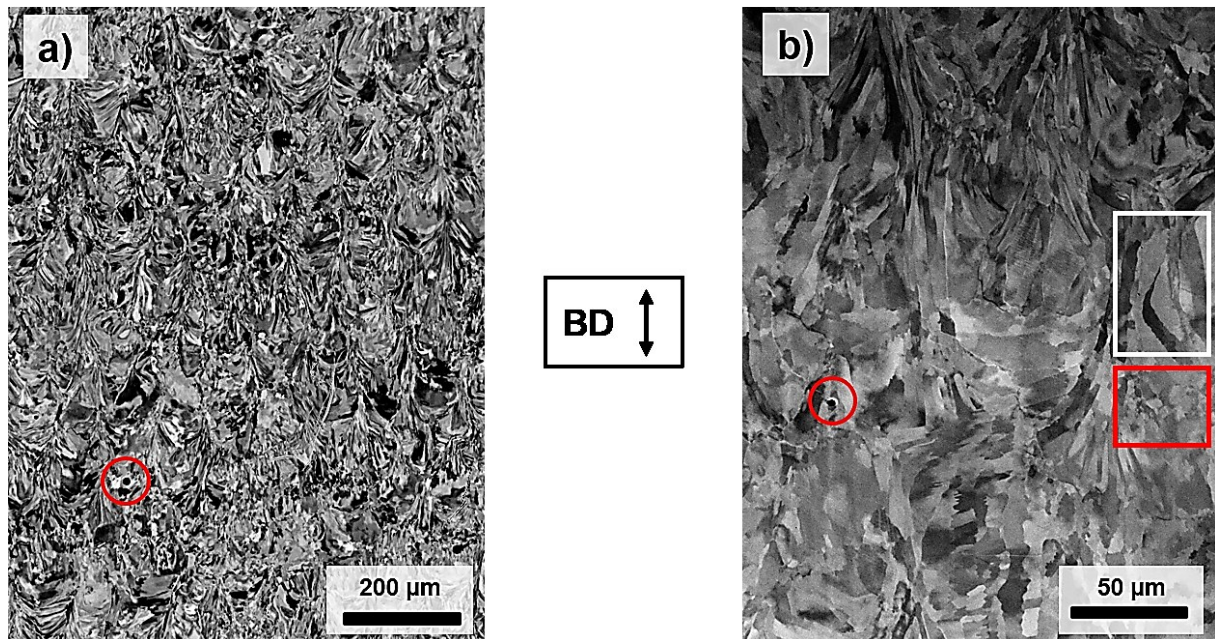


Fig. 2 Back-scattered electron SEM micrographs obtained at two different magnifications: (a) 250 \times , (b) 1000 \times . The red circles highlight pores being present at the surfaces studied. Areas of columnar and globular grains are highlighted by the white and red rectangles. The building direction is indicated by the arrow “BD”.

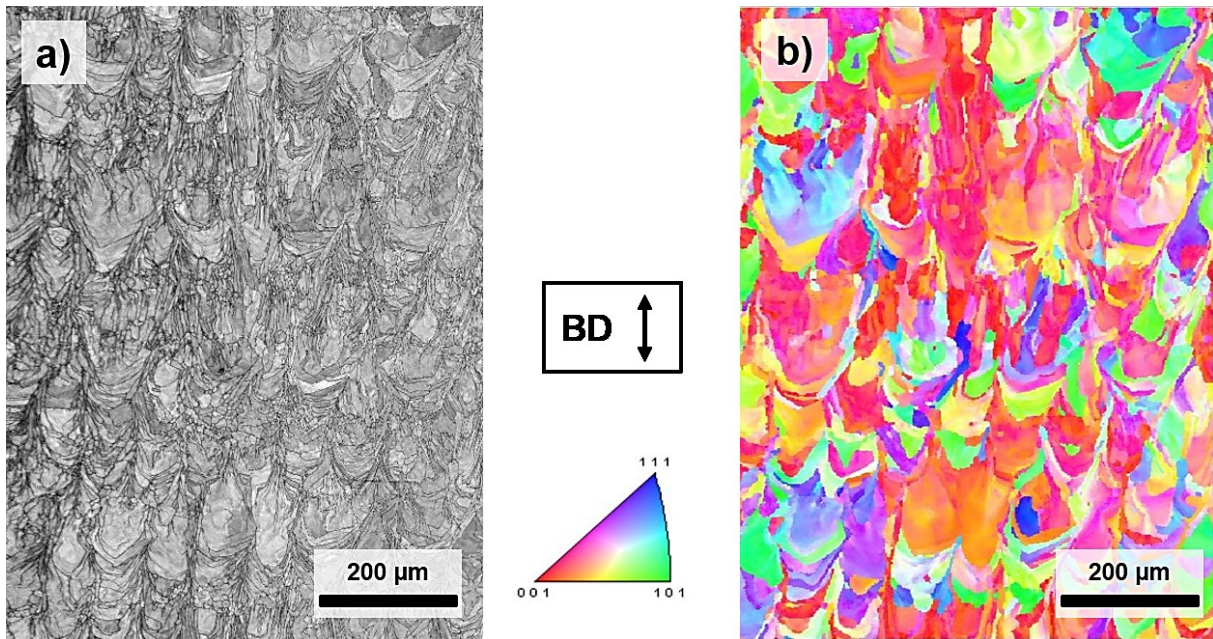


Fig. 3 SEM micrographs plotted in form of (a) an EBSD image quality map, (b) an inverse pole figure map. The grain orientations are plotted with respect to the building / loading direction indicated by the arrow “BD”.

Further texture analysis was conducted by XRD. The inverse pole figures highlighting the texture of the SLM Invar are displayed in Fig. 4 (1 indicating BD with respect to the SLM process / loading direction of the specimen, 2 the direction perpendicular to BD and 3 the transverse direction of the specimen, respectively). These results are in line with the findings of the EBSD measurements. Parallel to the build direction a strong texture towards the $\langle 001 \rangle$ pole is prevalent. For the other two directions depicted such strongly preferred orientation cannot be distinguished, even if the $\langle 011 \rangle$ pole is slightly increased in terms of intensity in the transverse direction of the specimen.

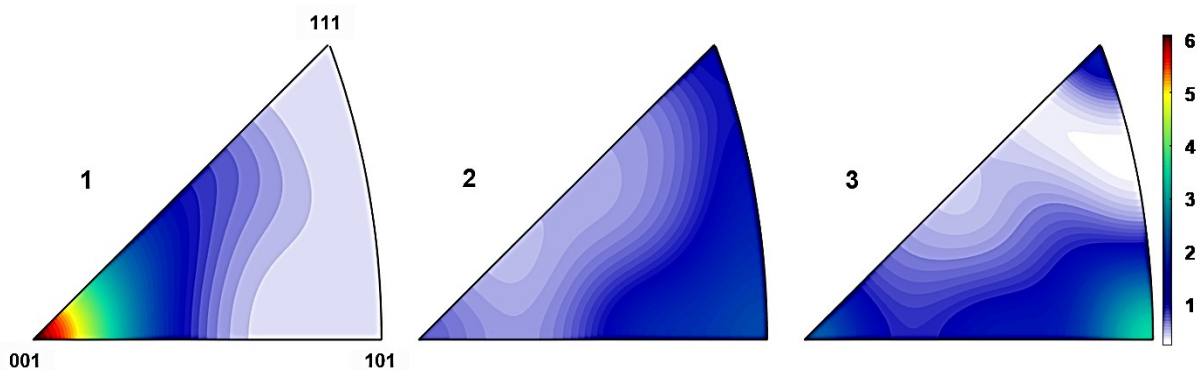


Fig. 4 Inverse pole figures obtained by XRD highlighting details on texture of the SLM processed Invar.

For defect characterization 2501 radiographs were captured non-destructively with a resolution of $1.95 \mu\text{m}/\text{voxel}$. The results including the reconstructed 3D-volume on the one hand and the corresponding subvolume for defect visualization within the reconstructed 3D-volume (transparent color illustration) on the other hand, are presented in Fig.5 (a) and (b) respectively. Total analyzed volume of the SLM Invar specimen was 5.07 mm^3 and the defined subvolume for porosity determination was chosen as large as possible ($260 \times 224 \times 975$ voxels). The total number of detected pores was 550 with an average pore diameter of $36 \mu\text{m}$ assuming a spherical defect. From these findings a porosity of 0.4 %, i.e., a relative density of 99.6 %, was calculated. A homogeneous distribution of the defects in the analyzed volume without any clusters or accumulations was observed. With respect to the pore morphology a sphericity of 0.94 (the value 1 is representative for an ideally spherical shape) could be determined.

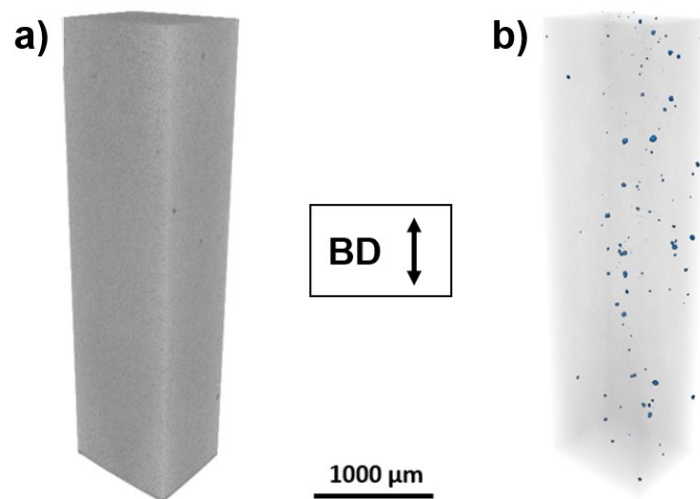


Fig. 5 Results obtained by X-ray μ -CT shown in form of (a) the reconstructed 3D-volume and (b) the corresponding defect distribution. The building direction is indicated by the arrow “BD”.

In order to analyze the overall homogeneity of the specimen, Vickers hardness measurements were carried out over the full length, i.e., the gauge length and the clamping

section. In total 451 individual measurements were carried out. The results obtained are shown in the hardness map in Fig. 6. The spot of each measurement point is represented by a black dot. A very homogeneous hardness distribution is clearly affirmed by the graph. The medium hardness was found to be approximately 158 HV1, whereas the maximum and minimum values were determined to 148 HV1 and 166 HV1, respectively.

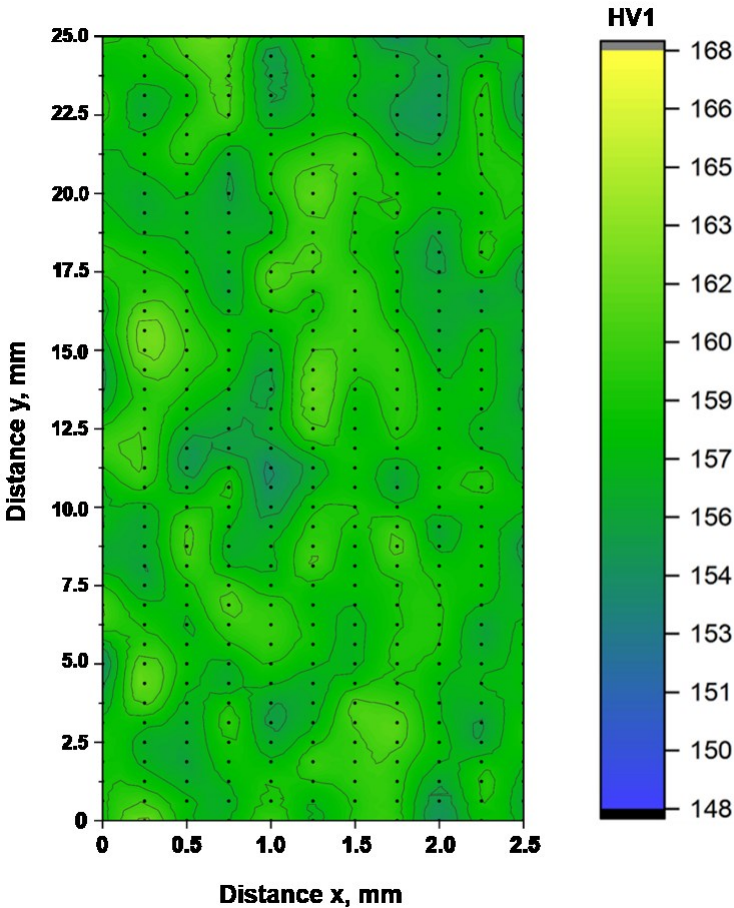


Fig. 6 Hardness map showing the hardness distribution over the full length of the SLM Invar specimen. Black dots represent the position of each single measurement.

3.2 Mechanical characterization

The behavior under monotonic tensile loading, displayed in Fig. 7, is shown by representative stress-strain curves obtained from two SLM Invar specimens, i.e., INVAR_1 and INVAR_2. The specimens INVAR_1 and INVAR_2 were taken from different cuboids in order to clearly reveal the reproducibility of the monotonic properties within different cuboids. From both curves a very similar, ductile material behavior can be derived. Upon initial yielding strain

hardening sets in. While YS and UTS, revealing values of 310 MPa and 445 MPa, respectively, are found to show no differences, the two specimen slightly differ in terms of elongation to failure. Compared to approximately 43 % for INVAR_1, specimen INVAR_2 shows a slightly higher elongation to failure of about 47 %.

The results obtained by fracture surface analysis for specimen INVAR_2 are shown in Fig. 8. The fracture surface exhibits a ductile, dimple-like fracture appearance, revealing yielding and a high amount of plastic deformation. As a result, the surface shows the well-known cup and cone fracture shape. Consistent with the results of microstructural analysis the fracture surface is characterized by the presence of a few spherical voids. However, in light of the relatively high elongation at fracture these pores seem not to affect the plastic deformability detrimentally.

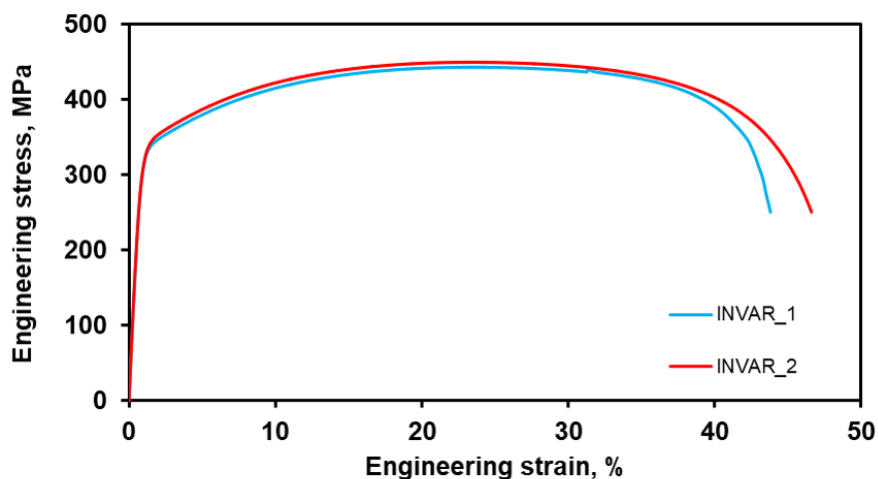


Fig. 7 Tensile stress-strain curves for two representative SLM Invar specimens.

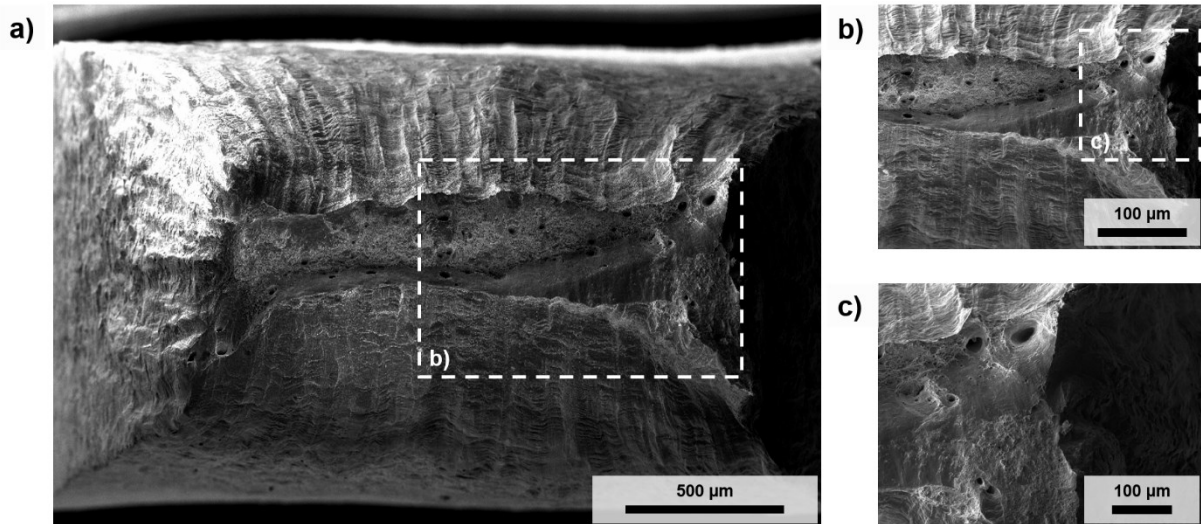
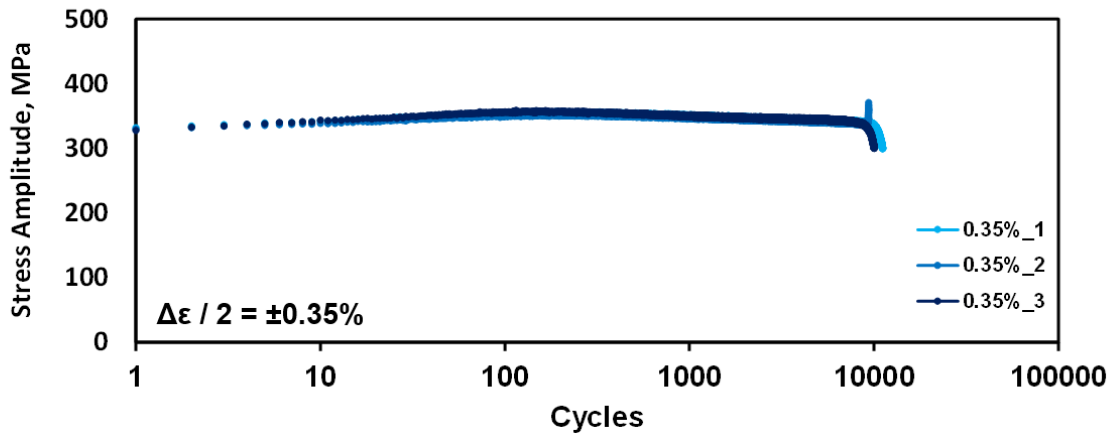


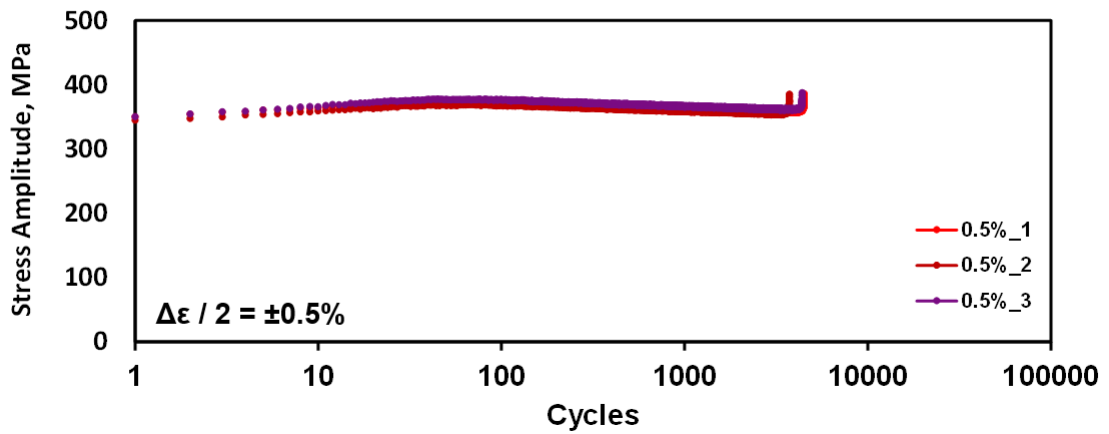
Fig. 8 SEM micrographs showing the fracture surface of the specimen INVAR_2; (a) fracture surface overview; (b and c) magnified details of the white dashed rectangles in (a) and (b), respectively.

Fig. 9 displays the cyclic deformation response (CDR) of the SLM Invar tested at various strain amplitudes, i.e., $\Delta\epsilon/2 = \pm 0.35\%$ (a), $\Delta\epsilon/2 = \pm 0.5\%$ (b) and $\Delta\epsilon/2 = \pm 0.65\%$ (c), respectively. In order to analyze the reproducibility and scatter behavior of the LCF response, three tests have been conducted for each strain amplitude considered. The CDRs demonstrate that with increasing strain amplitude fatigue lives decrease and stress amplitudes increase. The load was increased stepwise during the very first cycles in order to avoid buckling of the specimens. As a consequence, the prescribed strain amplitude was reached after approximately 25 to 75 cycles (in dependence of the strain amplitude) and the initial cycles of the CDRs are characterized by a steady increase of the stress amplitude. Irrespective of the strain amplitude, this initial behavior is followed by slight cyclic softening throughout the test, being more pronounced at the higher strain amplitudes. Comparing the different tests on each load level, a high reproducibility and no pronounced scatter can be seen with respect to the stress levels and fatigue lives of individual specimens (for all given strain amplitudes).

a)



b)



c)

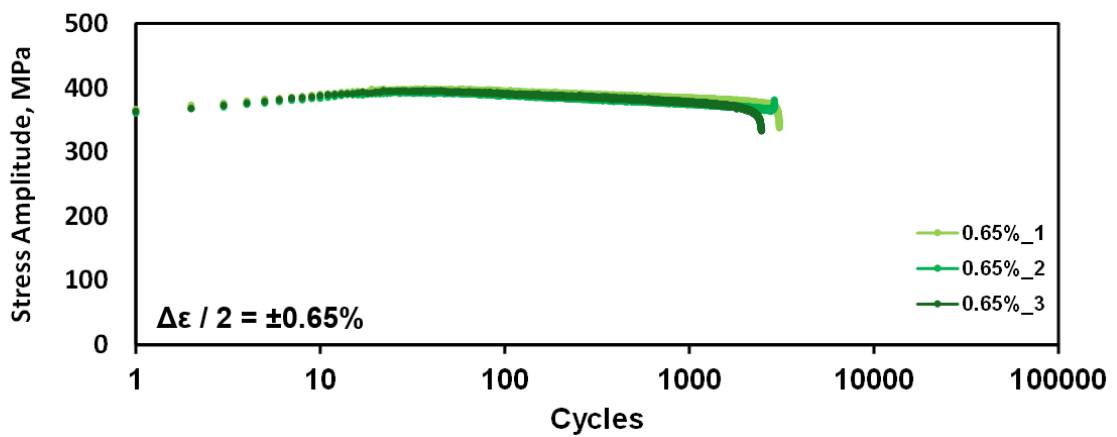


Fig. 9 Cyclic deformation response at room temperature for total strain amplitudes of $\Delta\epsilon/2 = \pm 0.35\%$ (a), $\Delta\epsilon/2 = \pm 0.5\%$ (b) and $\Delta\epsilon/2 = \pm 0.65\%$ (c) for the SLM processed Invar.

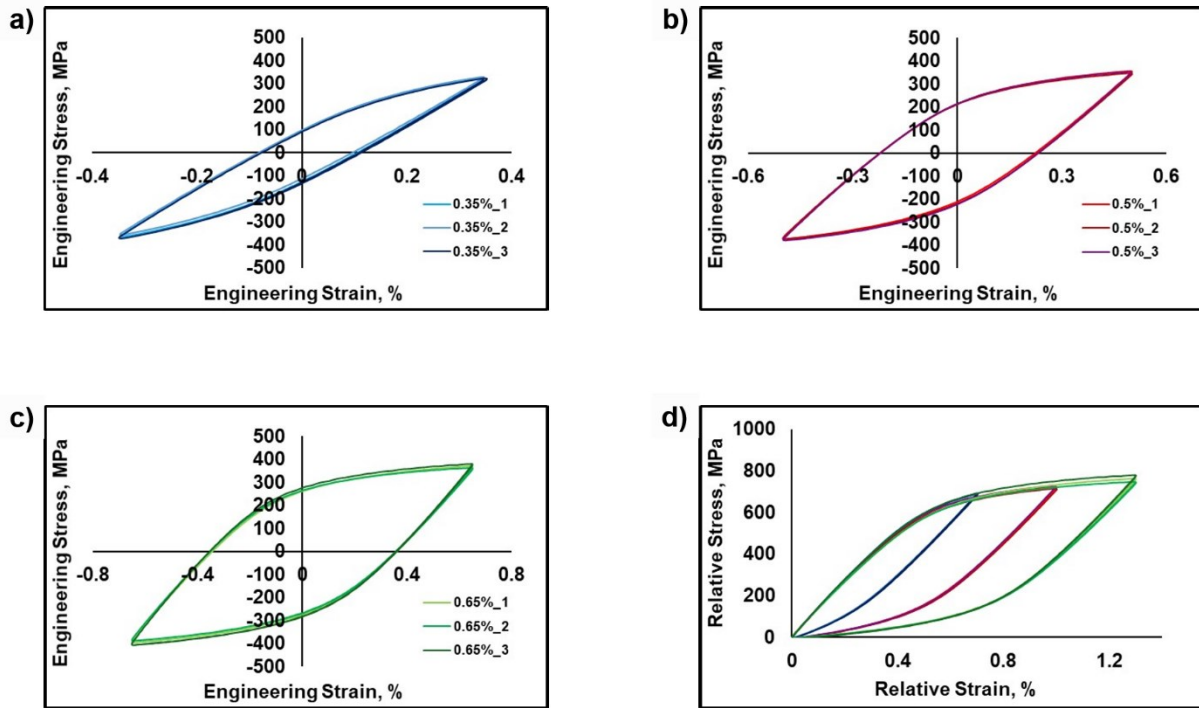
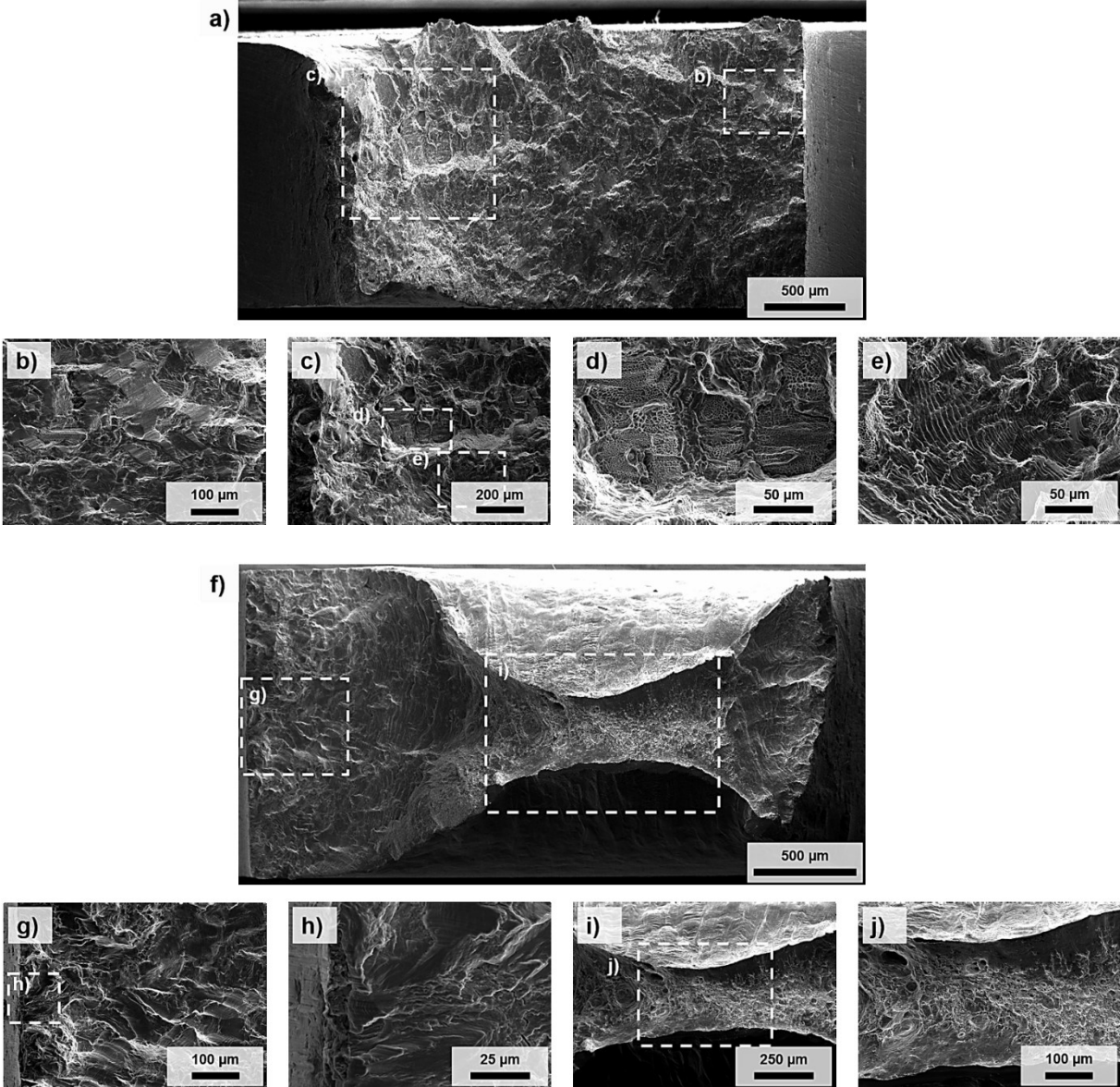


Fig. 10 Half-life hysteresis loops for the SLM processed Invar for total strain amplitudes of (a) $\Delta\epsilon/2 = \pm 0.35\%$, (b) $\Delta\epsilon/2 = \pm 0.5\%$, (c) $\Delta\epsilon/2 = \pm 0.65\%$ and (d) half-life hysteresis loops, plotted in relative coordinates, illustrating almost perfect Masing behavior for the SLM processed Invar.

The half-life hysteresis loops are displayed in Fig. 10 for each of the applied strain amplitudes, i.e., $\Delta\epsilon/2 = \pm 0.35\%$ (a), $\Delta\epsilon/2 = \pm 0.5\%$ (b) and $\Delta\epsilon/2 = \pm 0.65\%$ (c). In order to analyze these in terms of Masing behavior, Fig. 10 (d) depicts all half-life hysteresis loops plotted in relative coordinates. All hysteresis loops are characterized by significant contribution of plastic strain, as can be directly deduced from the hysteresis width. While the amount of plastic strain increases with increasing strain amplitude, the increase in the total stress amplitude is less pronounced. In line with the CDRs, the hysteresis curves of individual specimens tested on one strain level are almost congruent. Plotted in relative coordinates (Fig 10 (d)) the half-life hysteresis curves of all tests reveal a very symmetric shape. Furthermore, Masing behavior can be observed for the SLM Invar since the upper branches of the hysteresis loops are almost perfectly congruent.

Fracture surfaces for one tested specimen for each strain amplitude, i.e., $\Delta\epsilon/2 = \pm 0.35\%$ (a-e), $\Delta\epsilon/2 = \pm 0.5\%$ (f-j) and $\Delta\epsilon/2 = \pm 0.65\%$ (k-o), are shown in Fig. 11. Since similar characteristics were revealed for the other specimens tested on the same level, the depicted

fracture surfaces can be considered as representative. In general, well-known features for fatigue tested samples, i.e., an area of fatigue crack propagation being characterize by sub-micron fatigue striations (cf. Figs 11 (e), (g) and (m)), as well as an overload fracture area, characterized by a ductile, dimple-like structure (cf. Figs 11 (d), (j) and (n)), can be derived for all specimens and strain amplitudes, respectively. In line with the findings from fracture surface analysis of the tensile tested samples, the fracture surfaces of the fatigue specimen seem to be locally plastically deformed to a high degree. Such characteristics are promoted by the high ductility of the SLM Invar. In addition, the minor porosity revealed from the tensile specimen is confirmed by the fracture surfaces of the fatigued samples. Most importantly, pores being present on the fracture surfaces seem to have no detrimental impact on the LCF-behavior with respect to crack initiation. Fatigue cracks were initiated in direct vicinity of the surfaces (cf. Figs 11 (b), (h) and (m)), instead of being promoted by internal defects.



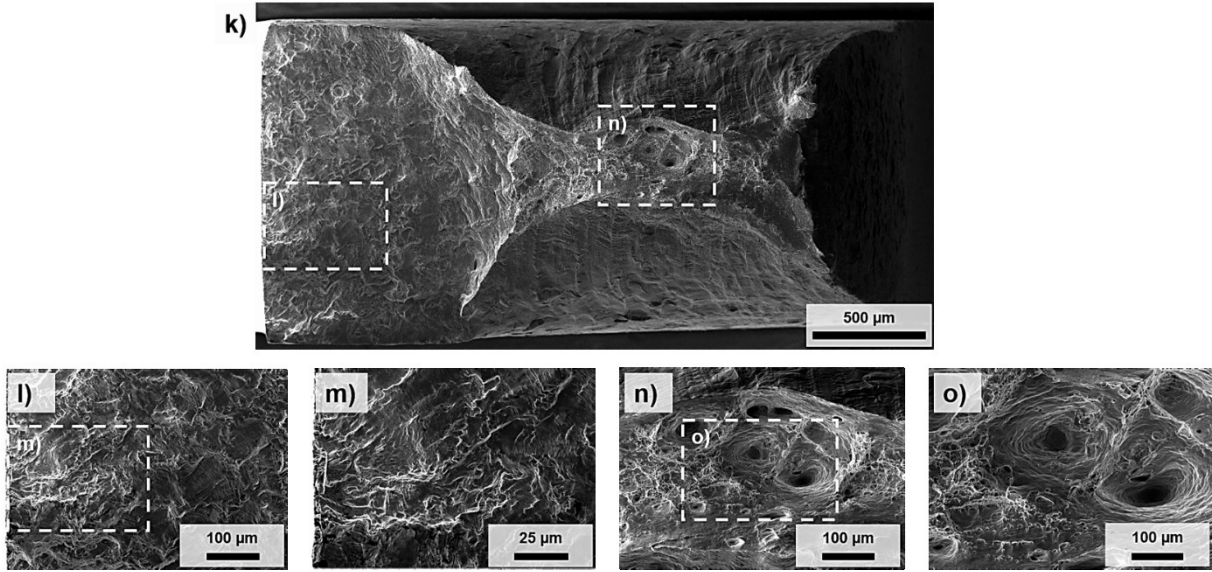


Fig. 11 SEM micrographs of several fracture surfaces: SLM Invar after fatigue testing at a strain amplitude of (a) $\Delta\varepsilon/2 = \pm 0.35\%$, (b) $\Delta\varepsilon/2 = \pm 0.5\%$ and (c) $\Delta\varepsilon/2 = \pm 0.65\%$. The subimages (b-e), (g-j) and (l-o) show magnified views of the accordingly marked white dashed rectangles.

The results of the dilatometer experiments, i.e., thermal expansion (a) and corresponding average linear CTE (b) are displayed in Fig. 12. Within a temperature range of 0°C - 100°C the specimen displacement highlighting thermal expansion is almost linear, leading to an almost constant CTE of $1.8 \times 10^{-6} \text{ K}^{-1}$ in this temperature range. In line with the change of the slope seen in Fig. 12 a, an increase of the CTE can be observed at temperatures above 100°C . This clearly indicates first changes of the magnetic properties. However, due to the limited temperature range considered, this change is not completed and the CTE continues to increase up to a value of approximately $4 \times 10^{-6} \text{ K}^{-1}$ when the maximum test temperature of 180°C is reached.

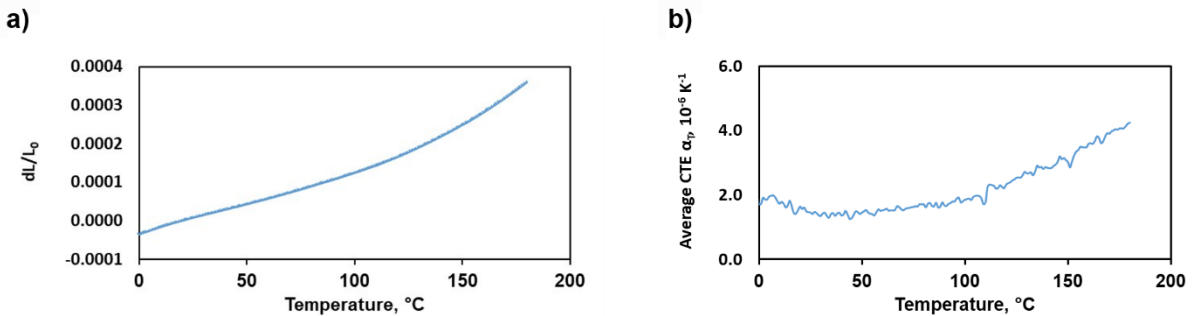


Fig. 12 (a) Thermal expansion and (b) corresponding average coefficient of thermal expansion for the SLM processed Invar.

4. Discussion

The main objective of the present work is the analysis of microstructure and mechanical properties, with an emphasis on the low-cycle fatigue behavior, of SLM processed Invar at ambient temperature.

Microstructural investigations revealed a bimodal microstructure homogeneously distributed within the entire specimen volume, being characterized by fan-like grain clusters consisting of columnar and globular grains. Such kind of microstructure arrangement is expected to be directly established by the conditions in the SLM process. This kind of microstructure has numerously been shown for alloys processed by SLM [35–38]. The average grain size of the SLM Invar was found to be 75 μm . In particular, a similar microstructure with respect to grain morphology for SLM processed Invar was reported by Harrison et al. [23] and Qui et al. [7]. In addition, a strong $\langle 001 \rangle$ crystallographic texture in build direction was revealed by EBSD investigations by the latter group. This is in line with the findings of the current study. Parallel to the building direction a strong texture towards the $\langle 001 \rangle$ pole with a maximum texture intensity of 6 was determined by EBSD and XRD measurements.

The results of defect characterization by 3D non-destructive analysis using X-ray μ -CT, shown in Fig. 5, revealed a homogeneous distribution of spherical defects. A porosity of 0.4 %, i.e., a relative density of 99.6 %, was calculated for the analyzed volume. The spherical shape as well as the corresponding pore size distribution (i.e., average pore diameter of 36 μm) of the defects indicates its source in hollow powder particles (the d_{50} value of the particle size distribution for the gas atomized powders was 29 μm). This explanation is further stressed by the nearly perfect sphericity of 0.94 calculated for the defects detected by μ -CT. The presence of hollow powder particles represents a typical and hardly avoidable phenomenon for components processed by AM based on gas-atomized precursor powder as numerously discussed in literature [39,40]. Additionally, porosities detected by μ -CT analysis could be attributed to local instabilities, likely keyholing, during SLM processing and, thus, directly to the process parameter set used. According to data reported in literature, however, the parameters chosen in present work are in a range leading to stable melting, homogeneous microstructure evolution as well as chemical homogeneity [12,24,25,27].

The results of the hardness measurements displayed in Fig. 6 reveal a hardness of 158 HV1 for the SLM Invar. Compared to conventionally processed and annealed Invar [4] the

hardness is higher by approximately 40 HV in the SLM processed condition. This significant increase can be rationalized based on the relatively small grain size induced by the SLM process in comparison to the rather large grains in conventionally manufactured counterparts. Due to the high cooling rate during the SLM process, less time is available for crystal growth, so that a basically fine-grained solidification microstructure is observed [41]. The hardness map shown in present work spans over the full specimen length, i.e., the gauge length and the grip section, revealing an excellent overall homogeneity. Thus, for large SLM Invar components without significant changes in their shape no gradient in the hardness distribution is expected. The selected process parameters are adequate to establish homogeneous microstructures all over the height of the produced part, and the solidification and cooling conditions seem to achieve a steady state already within the first few layers of the building process (only the layers below a build height of 2 mm were removed by specimen extraction and, thus, not incorporated in the hardness measurements).

The mechanical behavior of the SLM Invar was analyzed by tensile tests and low-cycle fatigue experiments. In literature, it was already indicated that the SLM process is known to generate residual stresses during the build process [42]. In order to exclude the influence of these residual stresses on the mechanical properties, especially the fatigue behavior of the SLM Invar, a stress relieving heat treatment was conducted. Thus, the behavior under monotonic and cyclic loading could just be correlated with the process-induced defects such as unmelted powder particles and keyholes. However, as the main scope of this work was to obtain first insights into the performance of SLM Invar under cyclic loading, the mechanical properties of the as-built condition were not studied. Clearly, this will be subject of follow-up studies. The material behavior under monotonic tensile loading was found to be very ductile. The two tensile tests conducted showed similar results with respect to YS and UTS (310 MPa and 445 MPa, respectively) and only differed with respect to elongation to fracture, where a maximum value of 47% was determined. Similar values were reported by Qui et al. [7] focusing on the effect of different laser scanning speeds. For a laser speed of 1000 mm/s, which is similar to the laser scanning speed of 900 mm/s used in present work, vertically built and heat treated specimen were characterized by an average YS and UTS of approximately 320 MPa and 445 MPa, respectively, and by elongations to fracture of about 30%. It has to be noted that the heat treatment route conducted by Qui et al. differed from that applied in the current study. However, applying different heat treatment parameters the authors did not observe significant changes in microstructure and consequently tensile properties [7]. Additionally, necking was reported for all tested specimen as similarly deduced from the results of post-tensile fracture surface analysis

shown in Fig. 8. Furthermore, similar values with respect to YS, UTS und elongations at fracture were reported by the group of Yakout et al. [22]. For a strongly textured material (as revealed by microstructural investigations, cf. Fig. 3 and Fig. 4), an anisotropic mechanical behavior has to be expected. Such effects have been already shown in literature [7]. However, analysis of the influence of the direction of the specimen was not in scope of the present work and, thus, specimens were only tested in BD. In first conclusion, tensile properties presented in this work are consistent with data reporting on SLM processed Invar in current literature. As a result it can be further concluded that, although minor amounts of porosity were detected, no significant process instabilities, i.e., insufficient melting or balling phenomena, in case of the parameter set used prevail.

In addition to the tensile tests the mechanical behavior of the SLM Invar was particularly studied by strain-controlled LCF tests focusing on various strain-amplitudes, i.e., $\Delta\varepsilon/2 = \pm 0.35\%$, $\Delta\varepsilon/2 = \pm 0.5\%$ and $\Delta\varepsilon/2 = \pm 0.65\%$. Three tests have been conducted for each strain amplitude considered. The CDRs were characterized by an initial increase of the stress due to a stepwise increase of the strain amplitude followed by a slight softening throughout the tests being more pronounced with increasing $\Delta\varepsilon/2$. This cyclic softening behavior is thought to result from a rearrangement and decrease in dislocation density, which cannot be compensated by any other mechanism inducing additional hardening (as shown in literature, e.g. [32,43]). However, experimental proof, e.g. provided by transmission electron microscopy, currently is missing and will be subject of future work. A similar cyclic softening behavior was also shown by Vinogradov et al. [28] in strain controlled fatigue tests conducted on a cold-rolled Invar alloy. Noticeably, irrespective of the strain amplitude the different tests for each strain level do not show any pronounced scatter in terms of stress amplitude and number of cycles to failure. Thus, a highly reproducible as well as predictable behavior under cyclic loading can be deduced for the SLM Invar being characterized by high damage tolerance. Eventually, this behavior can be rationalized based on the high ductility observed during tensile testing. An increasing plastic strain amplitude and decreasing number of cycles to failure with increasing total strain amplitude are captured well by the half-life hysteresis loops depicted in Fig. 10. The latter relation can be explained by the more pronounced contribution of plastic strain and plasticity induced damage, respectively, with increasing strain amplitude, derived from the hysteresis width. The high reproducibility of the investigations is further highlighted by the course of the hysteresis loops being nearly congruent for all test conducted on a given strain level. In addition, the upper branches of the hysteresis loops plotted in relative coordinates (cf. Fig. 10 (d)) are

absolutely congruent revealing perfect Masing behavior, i.e., a similar microstructure evolution independently of the strain amplitude imposed.

The ductile material behavior, already revealed by the results obtained upon monotonic loading, can likewise be deduced for cyclic loading by analysis of the results of post fatigue fractography shown in Fig. 11. All representative fracture surfaces depicted show fatigue crack propagation characterized by numerous fatigue striations, a ductile dimple-like structure and necking in the overload area. Minor amounts of porosity, a well-known phenomenon related to gas-atomized precursor powder in AM (cf. [44]), can be found on all fracture surfaces irrespective of the strain amplitude. Remarkably, initial fatigue cracking is not promoted by these defects but always takes place in the direct vicinity of the surface. As a direct result, the internal porosity seems to have minor impact on crack initiation and, thus, on the overall LCF properties of the SLM Invar, although only machined and ground specimens have been tested in present work. This is clearly contradictory to many other fatigue studies focusing on AM materials presented in literature. In their investigations on electron beam melted (EBM) and SLM processed Ti-6Al-4V respectively, Günther et al. [45] and Liu et al. [46] reported that crack initiation on a plane being oriented perpendicular to the loading direction was always promoted by defects such as lack-of-fusion (LoF) and porosity. On the contrary, in the present study a critical influence of process induced defects seems to be prevented by the ductile material behavior of the SLM Invar promoting high damage tolerance. A similar behavior under cyclic loading was also reported for SLM processed stainless steel 316L by the group of Leuders et al. [47]. They showed that due to the generally high ductility of 316L, stress-raisers could be compensated such that the alloy is relatively insensitive to micron-sized pores induced by the SLM process.

The thermal expansion characteristics of the SLM Invar were investigated in a temperature range between 0 °C and 180 °C as displayed in Fig. 12. Deduced from the almost linear specimen displacement, a constant CTE value was determined to $1.8 \times 10^{-6} \text{ K}^{-1}$ within the temperature range of 0 °C to 100 °C. Here, the CTE of SLM Invar is similar to conventionally processed (cast + forged) Invar [48], clearly proving the general presence of the Invar effect in case of the material characterized in the present study. However, even lower CTEs are reported in other studies focusing on as-built SLM processed Invar [9,23,24]. The deviation can be explained based on data reported by Harrison et al. [23]. According to their findings residual stresses, which are expected to be very low due to the specific heat treatment conducted in case of present work, are able to affect the magneto-volume contraction and, thus, can be a significant contributor to the reduced CTE of as-built SLM Invar specimens in direct

comparison to their stress-relieved counterparts. Another reason for lower CTEs is seen in the volume fraction and distribution of internal defects. Yakout et al. [24] showed for stress relieved specimens that void formation caused an increase in the magnetic dipole moment accompanied by a reduction of thermal expansion of these parts. Other studies [7,20] reported on anisotropic thermal expansion. However, the detailed analysis of the effects of residual stresses, defects and anisotropy on the CTE was out of the scope of the current study and, thus, needs to be thoroughly addressed in future work. Still, the results of the current study show that at least a CTE in the range of conventionally processed material is obtainable. In combination with the highly ductile behavior, an excellent damage tolerance under cyclic loading is observed, which paves the way for future industrial applications of SLM processed Invar.

5. Conclusions

The microstructure and mechanical behavior of SLM processed Invar under monotonic and particularly cyclic loading (LCF regime) at ambient temperature have been investigated. From the findings presented the following conclusions can be drawn:

1. The across the entire specimen volume generally homogeneous, bimodal microstructure is characterized by columnar and equiaxed grains with a strong $\langle 001 \rangle$ texture with respect to the build direction and an average grain size of 75 μm . A porosity of 0.4 %, i.e., a relative density of 99.6 %, was determined by X-ray $\mu\text{-CT}$.
2. Hardness distribution was found to be homogeneous without any gradient with respect to the build height of the produced parts due to the stability of the used process parameters. Monotonic tensile loading revealed a ductile material behavior being characterized by YS and UTS of 310 MPa and 445 MPa, respectively. Fracture surfaces exhibit a dimple-like fracture appearance with cup and cone shape.
3. The cyclic deformation response is characterized by minor cyclic softening. No pronounced scatter is found with respect to stress amplitude and number of cycles to failure, i.e., a highly reproducible, damage tolerant behavior under cyclic loading is determined. Half-life hysteresis loops reveal perfect Masing behavior, i.e., similar microstructure evolution independently of the imposed strain amplitude.
4. Post fatigue fractography reveals crack initiation on the (machined and ground) surfaces, although a minor amount of porosity in the interior, presumably due to hollow powder particles and keyholing effects, is detectable. Thus, these process induced

defects seem to have no detrimental impact on the LCF properties, eventually promoting a damage tolerant material behavior under cyclic loading.

5. SLM processed Invar shows a sufficiently low thermal expansion behavior in the temperature range within 0 °C to 180 °C. Between 0 °C and 100 °C a CTE of $1.8 \times 10^{-6} \text{ K}^{-1}$, very similar to conventionally processed Invar, is determined.

Acknowledgements

The authors would like to thank Mr. J. Fischer for specimen preparation, Dr.-Ing. A. Liehr for his help with texture analysis, Mr. T. Oevermann for conducting the hardness measurements and Mr. R. Diederich for performing the fracture surface investigations.

References

- [1] C.E. Guillaume, Invar and Its Applications, *Nature* 71 (1904) 134–139.
- [2] T. Yokoyama, K. Eguchi, Anharmonicity and quantum effects in thermal expansion of an Invar alloy, *Physical review letters* 107 (2011) 65901.
- [3] Y. Ishikawa, N. Miura (Eds.), *Physics and Engineering Applications of Magnetism*, Springer, Berlin, Heidelberg, 1991.
- [4] W.D. Callister, D.G. Rethwisch, *Materials science and engineering: SI version*, 9th ed., Wiley, Hoboken, NJ, 2015.
- [5] M. Shiga, Invar alloys, *Current Opinion in Solid State and Materials Science* 1 (1996) 340–348.
- [6] J.L. Corbacho, J.C. Suárez, F. Molleda, Welding of invar Fe-36Ni alloy for tooling of composite materials, *Welding International* 12 (1998) 966–971.
- [7] C. Qiu, N.J.E. Adkins, M.M. Attallah, Selective laser melting of Invar 36, *Acta Mater.* 103 (2016) 382–395.
- [8] S.-H. Kim, S.-G. Choi, W.-K. Choi, E.-S. Lee, Surface characteristics of Invar alloy according to micro-pulse electrochemical machining, *Mater. Tehnol.* 51 (2017) 745–749.
- [9] H. Asgari, M. Salarian, H. Ma, A. Olubamiji, M. Vlasea, On thermal expansion behavior of invar alloy fabricated by modulated laser powder bed fusion, *Materials & Design* 160 (2018) 895–905.
- [10] S.-H. Kim, H.-J. Sohn, Y.-C. Joo, Y.-W. Kim, T.-H. Yim, H.-Y. Lee, T. Kang, Effect of saccharin addition on the microstructure of electrodeposited Fe–36 wt.% Ni alloy, *Surface and Coatings Technology* 199 (2005) 43–48.
- [11] B. Mills, A.H. Redford, *Machinability of Engineering Materials*, Springer Netherlands, Dordrecht, 1983.
- [12] M. Yakout, A. Cadamuro, M.A. Elbestawi, S.C. Veldhuis, The selection of process parameters in additive manufacturing for aerospace alloys, *Int J Adv Manuf Technol* 92 (2017) 2081–2098.
- [13] M. Schmidt, M. Merklein, D. Bourell, D. Dimitrov, T. Hausotte, K. Wegener, L. Overmeyer et al., Laser based additive manufacturing in industry and academia, *CIRP Annals* 66 (2017) 561–583.
- [14] D. Herzog, V. Seyda, E. Wycisk, C. Emmelmann, Additive manufacturing of metals, *Acta Mater.* 117 (2016) 371–392.
- [15] L.E. Murr, S.M. Gaytan, D.A. Ramirez, E. Martinez, J. Hernandez, K.N. Amato, P.W. Shindo et al., Metal Fabrication by Additive Manufacturing Using Laser and Electron Beam Melting Technologies, *Journal of Materials Science & Technology* 28 (2012) 1–14.

- [16] J.J. Lewandowski, M. Seifi, Metal Additive Manufacturing, *Annu. Rev. Mater. Res.* 46 (2016) 151–186.
- [17] C.Y. Yap, C.K. Chua, Z.L. Dong, Z.H. Liu, D.Q. Zhang, L.E. Loh, S.L. Sing, Review of selective laser melting, *Applied Physics Reviews* 2 (2015) 41101.
- [18] P. Li, D.H. Warner, A. Fatemi, N. Phan, Critical assessment of the fatigue performance of additively manufactured Ti–6Al–4V and perspective for future research, *International Journal of Fatigue* 85 (2016) 130–143.
- [19] Terry Wohlers, Wohlers report 2015: 3D printing and additive manufacturing state of the industry annual worldwide progress report, Wohlers Associates, Fort Collins (Colo.), 2015.
- [20] K. Moussaoui, W. Rubio, M. Mousseigne, T. Sultan, F. Rezai, Effects of Selective Laser Melting additive manufacturing parameters of Inconel 718 on porosity, microstructure and mechanical properties, *Materials Science and Engineering: A* 735 (2018) 182–190.
- [21] E. Liverani, S. Toschi, L. Ceschini, A. Fortunato, Effect of selective laser melting (SLM) process parameters on microstructure and mechanical properties of 316L austenitic stainless steel, *Journal of Materials Processing Technology* 249 (2017) 255–263.
- [22] R. Rashid, S.H. Masood, D. Ruan, S. Palanisamy, R.A. Rahman Rashid, M. Brandt, Effect of scan strategy on density and metallurgical properties of 17-4PH parts printed by Selective Laser Melting (SLM), *Journal of Materials Processing Technology* 249 (2017) 502–511.
- [23] N.J. Harrison, I. Todd, K. Mumtaz, Thermal expansion coefficients in Invar processed by selective laser melting, *J. Mater. Sci.* 52 (2017) 10517–10525.
- [24] M. Yakout, M.A. Elbestawi, S.C. Veldhuis, A study of thermal expansion coefficients and microstructure during selective laser melting of Invar 36 and stainless steel 316L, *Additive Manufacturing* 24 (2018) 405–418.
- [25] M. Yakout, M.A. Elbestawi, S.C. Veldhuis, Density and mechanical properties in selective laser melting of Invar 36 and stainless steel 316L, *Journal of Materials Processing Technology* 266 (2019) 397–420.
- [26] N. Khanna, S. Mistry, R.A. Rahman Rashid, M.K. Gupta, Investigations on density and surface roughness characteristics during selective laser sintering of Invar-36 alloy, *Mater. Res. Express* 6 (2019) 86541.
- [27] K. Wei, Q. Yang, B. Ling, X. Yang, H. Xie, Z. Qu, D. Fang, Mechanical properties of Invar 36 alloy additively manufactured by selective laser melting, *Materials Science and Engineering: A* 772 (2020) 138799.
- [28] A. Vinogradov, S. Hashimoto, V.I. Kopylov, Enhanced strength and fatigue life of ultra-fine grain Fe–36Ni Invar alloy, *Materials Science and Engineering: A* 355 (2003) 277–285.
- [29] R. Molaei, A. Fatemi, Fatigue Design with Additive Manufactured Metals, *Procedia Engineering* 213 (2018) 5–16.
- [30] F. Bachmann, R. Hielscher, H. Schaeben, Texture Analysis with MTEX – Free and Open Source Software Toolbox, *SSP* 160 (2010) 63–68.
- [31] FEI SAS, a part of Thermo Fisher Scientific, Thermo Scientific Avizo Software 9 - User's Guide.
- [32] T. Niendorf, C. Lotze, D. Canadinc, A. Frehn, H.J. Maier, The role of monotonic pre-deformation on the fatigue performance of a high-manganese austenitic TWIP steel, *Materials Science and Engineering: A* 499 (2009) 518–524.
- [33] R.K. Singh, J.K. Sahu, S. Tarafder, Strain rate effect on cyclic deformation behaviour of advanced ultra-supercritical boiler grade wrought Ni-based superalloy IN740H at 760 °C, *Materials Science and Engineering: A* 658 (2016) 272–279.
- [34] S.K. Paul, N. Stanford, A. Taylor, T. Hilditch, The effect of low cycle fatigue, ratcheting and mean stress relaxation on stress–strain response and microstructural development in a dual phase steel, *International Journal of Fatigue* 80 (2015) 341–348.

- [35] L. Thijs, M.L. Montero Sistiaga, R. Wauthle, Q. Xie, J.-P. Kruth, J. van Humbeeck, Strong morphological and crystallographic texture and resulting yield strength anisotropy in selective laser melted tantalum, *Acta Mater.* 61 (2013) 4657–4668.
- [36] T. Niendorf, S. Leuders, A. Riemer, H.A. Richard, T. Tröster, D. Schwarze, Highly Anisotropic Steel Processed by Selective Laser Melting, *Metall and Materi Trans B* 44 (2013) 794–796.
- [37] T. Niendorf, F. Brenne, P. Krooß, M. Vollmer, J. Günther, D. Schwarze, H. Biermann, Microstructural Evolution and Functional Properties of Fe-Mn-Al-Ni Shape Memory Alloy Processed by Selective Laser Melting, *Metall and Mat Trans A* 47 (2016) 2569–2573.
- [38] M. L. Montero Sistiaga, S. Nardone, C. Hautfenne, J. Van Humbeeck, Effect of heat treatment of 316L stainless steel produced by selective laser melting (SLM), 2016 Annual International Solid Freeform Fabrication Symposium, Austin, Texas, USA (2016) 558–565.
- [39] C. Qiu, N.J.E. Adkins, M.M. Attallah, Microstructure and tensile properties of selectively laser-melted and of HIPed laser-melted Ti–6Al–4V, *Materials Science and Engineering: A* 578 (2013) 230–239.
- [40] B. Zhang, Y. Li, Q. Bai, Defect Formation Mechanisms in Selective Laser Melting: A Review, *Chin. J. Mech. Eng.* 30 (2017) 1476.
- [41] D.D. Gu, W. Meiners, K. Wissenbach, R. Poprawe, Laser additive manufacturing of metallic components, *International Materials Reviews* 57 (2013) 133–164.
- [42] Z.-C. Fang, Z.-L. Wu, C.-G. Huang, C.-W. Wu, Review on residual stress in selective laser melting additive manufacturing of alloy parts, *Optics & Laser Technology* 129 (2020) 106283.
- [43] Z. Zhang, Z. Hu, S. Schmauder, M. Mlikota, K. Fan, Low-Cycle Fatigue Properties of P92 Ferritic-Martensitic Steel at Elevated Temperature, *J. of Materi Eng and Perform* 25 (2016) 1650–1662.
- [44] S. Tammias-Williams, H. Zhao, F. Léonard, F. Derguti, I. Todd, P.B. Prangnell, XCT analysis of the influence of melt strategies on defect population in Ti–6Al–4V components manufactured by Selective Electron Beam Melting, *Materials Characterization* 102 (2015) 47–61.
- [45] J. Günther, D. Krewerth, T. Lippmann, S. Leuders, T. Tröster, A. Weidner, H. Biermann et al., Fatigue life of additively manufactured Ti–6Al–4V in the very high cycle fatigue regime, *International Journal of Fatigue* 94 (2017) 236–245.
- [46] Q.C. Liu, J. Elambasseril, S.J. Sun, M. Leary, M. Brandt, P.K. Sharp, The Effect of Manufacturing Defects on the Fatigue Behaviour of Ti-6Al-4V Specimens Fabricated Using Selective Laser Melting, *AMR 891-892* (2014) 1519–1524.
- [47] S. Leuders, T. Lieneke, S. Lammers, T. Tröster, T. Niendorf, On the fatigue properties of metals manufactured by selective laser melting – The role of ductility, *J. Mater. Res.* 29 (2014) 1911–1919.
- [48] J.R. Davis, *Alloying: Understanding the basics*, ASM International, Materials Park, Ohio, 2011.